Astronomy & Astrophysics manuscript no. nugas2
March 14, 2014
© ESO 2014

arXiv:1401.4120v2 [astro-ph.GA] 13 Mar 2014

ALMA reveals the feeding of the Seyfert 1 nucleus in NGC 1566 ⋆

F. Combes[1], S. García-Burillo[2], V. Casasola[3], L. K. Hunt[4], M. Krips[5], A. J. Baker[6], F. Boone[7], A. Eckart[8], I. Marquez[9], R. Neri[5], E. Schinnerer[10], and L. J. Tacconi[11]

[1] Observatoire de Paris, LERMA (CNRS:UMR8112), 61 Av. de l'Observatoire, F-75014, Paris, France e-mail: francoise.combes@obspm.fr
[2] Observatorio Astronómico Nacional (OAN)-Observatorio de Madrid, Alfonso XII, 3, 28014-Madrid, Spain
[3] INAF – Istituto di Radioastronomia & Italian ALMA Regional Centre, via Gobetti 101, 40129, Bologna, Italy
[4] INAF - Osservatorio Astrofisico di Arcetri, Largo E. Fermi, 5, 50125, Firenze, Italy
[5] IRAM, 300 rue de la Piscine, Domaine Universitaire, F-38406 Saint Martin d'Hères, France
[6] Dep. of Physics & Astronomy, Rutgers, the State University of New Jersey, 136 Frelinghuysen road, Piscataway, NJ 08854, USA
[7] CNRS, IRAP, 9 Av. colonel Roche, BP 44346, 31028, Toulouse Cedex 4, France
[8] I. Physikalisches Institut, Universität zu Köln, Zülpicher Str. 77, 50937, Köln, Germany
[9] Instituto de Astrofísica de Andalucía (CSIC), Apdo 3004, 18080 Granada, Spain
[10] Max-Planck-Institut für Astronomie (MPIA), Königstuhl 17, 69117 Heidelberg, Germany
[11] Max-Planck-Institut für extraterrestrische Physik, Giessenbachstr. 1, Garching bei München, Germany

Received 2014/ Accepted 2014

ABSTRACT

We report ALMA observations of CO(3-2) emission in the Seyfert 1 galaxy NGC 1566, at a spatial resolution of 25 pc. Our aim is to investigate the morphology and dynamics of the gas inside the central kpc, and to probe nuclear fueling and feedback phenomena. NGC 1566 has a nuclear bar of 1.7 kpc radius and a conspicuous grand design spiral starting from this radius. The ALMA field of view, of diameter 0.9 kpc, lies well inside the nuclear bar and reveals a molecular trailing spiral structure from 50 to 300 pc in size, which is contributing to fuel the nucleus, according to its negative gravity torques. The spiral starts with a large pitch angle from the center and then winds up in a pseudo-ring at the inner Lindblad resonance (ILR) of the nuclear bar. This is the first time that a trailing spiral structure is clearly seen driving the gas inwards inside the ILR ring of the nuclear bar. This phenomenon shows that the massive central black hole has a significant dynamical influence on the gas, triggering its fueling. The gaseous spiral is well correlated with the dusty spiral seen through extinction in HST images, and also with a spiral feature emitting 0.87mm continuum. This continuum emission must come essentially from cold dust heated by the interstellar radiation field. The HCN(4-3) and HCO^+(4-3) lines were simultaneously mapped and detected in the nuclear spiral. The HCO^+(4-3) line is 3 times stronger than the HCN(4-3), as expected when star formation excitation dominates over active galactic nucleus (AGN) heating. The CO(3-2)/HCO^+(4-3) integrated intensity ratio is ∼ 100. The molecular gas is in remarkably regular rotation, with only slight non-circular motions at the periphery of the nuclear spiral arms. These perturbations are quite small, and no outflow nor AGN feedback is detected.

Key words. Galaxies: active — Galaxies: Individual: NGC 1566 — Galaxies: ISM — Galaxies: kinemativs and dynamics — Galaxies: nuclei — Galaxies: spiral

1. Introduction

An astrophysical problem that has seen much progress in recent years is understanding how active galactic nuclei (AGN) are fueled in galaxies, and how the energy generated by the active nucleus can in turn regulate gas accretion (e.g. Croton et al. 2006; Sijacki et al. 2007). This has important implications for the co-evolution of galaxies and black holes, which is observed through the now well established M-σ relation (e.g., Gültekin et al. 2009). Driving sufficient gas towards the center to sustain nuclear activity requires the removal of angular momentum from the gas, and therefore the creation of large non-axisymmetries. The invoked dynamical mechanisms depend on the scale in question: at 10 kpc scales, torques are produced by galaxy interactions and mergers (e.g., Hopkins et al. 2006; di Matteo et al. 2008); at kpc scales, bar instabilities, either internally driven by secular evolution or triggered by companions, can first feed a central starburst and then fuel the massive black hole (García-Burillo et al. 2005). At 300 pc scales, the "bars within bars" scenario (e.g., Shlosman et al. 1989), together with m=1 instabilities, takes over as a dynamical mechanism; however, our IRAM-PdBI observational program NUclei of GAlaxies (NUGA) has revealed smoking-gun evidence of AGN fueling only in one third of the galaxies observed (García-Burillo & Combes 2012). This might be due to nuclear star formation or AGN feedback driving gas outflows that stop the fueling; galaxies will then undergo successive periods of fueling and starvation, and might be found in a feeding phase at 300 pc scales only one third of the time. Other mechanisms could contribute to the fueling, especially towards the center of galaxies: viscous torques, from dense gas in regions of large shear, or dynamical friction of massive clouds against the old bulge stars (e.g. Combes 2002, Jogee 2006). At the radii of interest, though, these are slower than gravity torques, when present.

To go beyond these scales and explore the molecular ISM 30 pc to 300 pc scales in local AGN host galaxies, we have undertaken an observing campaign with ALMA, the only instrument able to probe the molecular emission with enough spa-

Send offprint requests to: F. Combes
⋆ Based on observations carried out with ALMA in cycle 0.

tial resolution and sensitivity. Observations and simulations are advancing together, since it is only now that we can simulate coherently these scales with successive zoom-in re-simulations (e.g., Hopkins & Quataert 2010; Renaud et al. 2013). At 30 pc scales, simulations suggest fueling involves a cascade of dynamical instabilities (m=2, m=1), and the formation of a thick gas disk similar to a torus, subject to bending and warping instabilities (Hopkins et al. 2012). Since the gas concentration becomes large, the gas is highly unstable, clumpy and turbulent. Dynamical friction can then drive these massive clumps to the nucleus. Simulations reveal episodic feeding with 10Myr timescales (10 pc) or even lower (0.1pc). These fueling episodes are then quenched by either star formation winds or AGN outflows.

Recently, high velocity outflows have been discovered in the molecular gas of nearby AGN (Feruglio et al. 2010; Sturm et al. 2011; Alatalo et al. 2011; Dasyra & Combes 2012). Outflows have been traced for a long time in ionized or atomic gas (Rupke et al. 2005; Riffel & Storchi-Bergmann 2011). With our ALMA cycle 0 data, we have been able to confirm that molecular outflows are also seen in low-luminosity AGN. The outflow revealed in the Seyfert 2 NGC 1433 is the least massive molecular outflow ever seen in galaxy nuclei (Combes et al. 2013). In the prototypical Seyfert 2 NGC 1068, a clear molecular ouflow has also been detected, entrained by the AGN radio jets (Krips et al. 2011; García-Burillo et al. 2010, 2014 in prep.).

These high angular resolution results have shown that fueling and feedback phases can occur simultaneously. Gas is inflowing in the plane, with some also outflowing along the minor axis at some angle with the plane. In NGC 1433, the CO map reveals a nuclear gaseous spiral structure inside the 460 pc-radius nuclear ring encircling the nuclear stellar bar. The nuclear spiral winds up in a pseudo-ring at ~200 pc radius, which might correspond to the inner Lindblad resonance (ILR). In spite of the presence of gas in rings at both outer and inner ILRs, some gas is finding its way to the center. In both of these Seyfert 2 galaxies, dust continuum emission is detected in a small nuclear disk, which might be interpreted as the molecular torus (Combes et al. 2013). In NGC 1068, the AGN is clearly off-center with respect to the torus, implying an m=1 perturbation (García-Burillo et al. 2014 in prep.).

In this paper, we present ALMA cycle 0 observations in the CO(3-2) line of the Seyfert 1 NGC 1566, with a spatial resolution of ~ 25 pc. Its proximity (10 Mpc) and small inclination of 35° make NGC 1566 an ideal target to test and refine scenarios of AGN feeding and feedback, and discover new phenomena controlling gas structures and dynamics within 100 pc, where the dynamical time-scale is smaller than 3 Myr (for V_{rot} ~ 200 km/s). In the next subsection, all relevant characteristics of NGC 1566 are described. Observations are detailed in Section 2 and results in Section 3. The interpretation in term of torques is discussed in Section 4, and conclusions are drawn in Section 5.

1.1. NGC 1566

NGC 1566, a nearly face-on spiral galaxy, is the brightest member of the Dorado group (Agüero et al. 2004; Kilborn et al 2005). It has an intermediate strength bar type (SAB), and two strongly contrasted spiral arms, emanating from the bar and winding up in an outer pseudo ring. The remarkable grand-design spiral has inspired special studies of its logarithmic arm structure (Elmegreen & Elmegreen 1990; Korchagin et al. 2000). There are two sets of spiral arms (see Fig. 1): the first set starts at the end of the nuclear bar of about 35″=1.7 kpc in radius, better seen

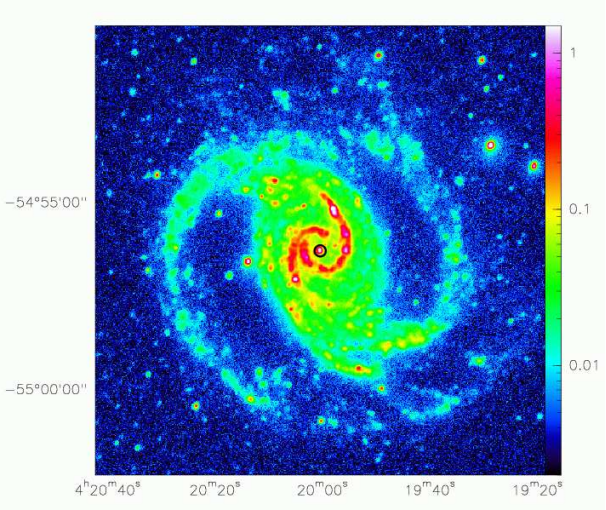

Fig. 1. *GALEX*-NUV image of NGC 1566, showing the two sets of spiral arm structures at large scales. The ALMA field of view (9″ radius) is shown as the black circle in the center. The image is a square of 12′ size. The color scale is in log.

in the near infrared (Hackwell & Schweizer 1983). These arms then wind up in a ring, with kinks and a circle of star formation, identified as the corotation of the spiral pattern (Elmegreen & Elmegreen 1990). A second weaker set of spiral arms then winds up in an outer pseudo ring, identified as the outer Lindblad resonance. The inner Lindblad resonance of the spiral might correspond to the end of the nuclear bar, and therefore the corotation of the bar. Inside this ILR, there is a deficiency of HII regions (Comte & Duquennoy 1982).

NGC 1566 is a low-luminosity AGN, classified as Seyfert, although its precise position between Seyfert 1 and 2 varies in the literature. More specifically, its nuclear spectrum varies from Seyfert 1 in its most active phases to Seyfert 2 at minimum activity (Alloin et al. 1985). It has many characteristics of Seyfert 1 galaxies/AGN: a bright central point-like source (Malkan et al. 1998), relatively broad [FeII] line emission in the Broad Line Rregion (Reunanen et al. 2002), characteristic variability on scales of months (Alloin et al. 1986), and an X-ray point-source nuclear luminosity between 2-10 keV of 7×10^{40} erg/s (Levenson et al. 2009). The nucleus is known to be variable from X-rays to IR bands (Alloin et al. 1986; Baribaud et al. 1992; Glass 2004). These variations have been interpreted as instabilities in a thin accretion disk (Abramowicz et al. 1986). The mass of the NGC 1566 black hole has been estimated to be 8.3×10^6 $M_\odot$ by the M-σ relation and the measured stellar velocity dispersion at the center (Woo & Urry 2002). From its bolometric luminosity, its Eddington ratio can be estimated as 0.096 (cf Table 1). HST [OIII] images show a one-sided ionization cone towards the south-east (Schmitt & Kinney 1996). VISIR images (Reunanen et al. 2010) reveal a dominant central unresolved source with size FWHM < 15 pc at 11.8 μm. Both large-scale and nuclear radio emission is seen in NGC 1566 (Harnett 1984, 1987). The atomic gas (HI) dynamics have been investigated with the ATCA interferometer by Walsh (2004), with a spatial resolution of ~ 30″. There is a 30″x50″ HI hole towards the center, where the gas becomes mostly molecular. The CO(1-0) and (2-1) lines have been mapped by Bajaja et al. (1995) with the SEST telescope, and are detected out to 60″radius. Excited molecular hydrogen has been detected through its ro-vibrational lines at 2μm (Reunanen et al. 2002). The H_2 excitation is not by UV fluorescence but

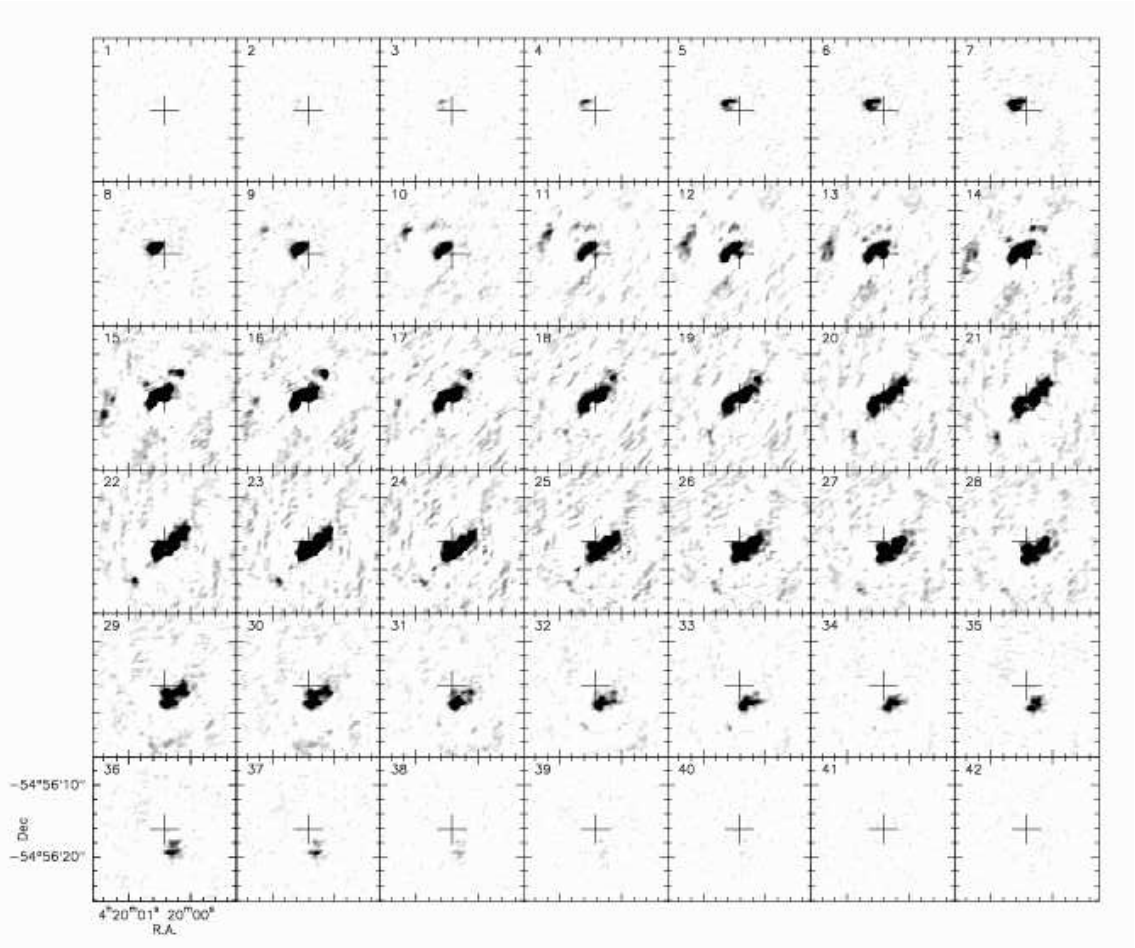

Fig. 2. Channel maps of CO(3-2) emission in the center of NGC 1566. Each of the 42 panels is 20″ in size. Channels are separated by 10.15 km/s. They are plotted from V_{hel}=1302 (top left) to 1718.15 km/s (bottom right). The synthesized beam is 0.64″ x 0.43″ (PA=123°). The phase center of the observations (marked by a 4″ cross) is given in Table 1. The grey scale is linear, between 1 and 30 mJy/beam. The central channels are saturated to better show the extent of the emission.

through thermal UV heating. The contribution from star formation is less than 10%, and the dominant H_2 excitation mechanism is collisional via shocks. The derived H_2 masses observed out to 2″ from the center are $90M_\odot$ along the ionised cone and $110M_\odot$ perpendicular to it.

The distance of NGC 1566 is still subject to large uncertainty. The measured heliocentric velocity of 1504 km/s, correcting for the solar motion inside the Local Group and accounting for the Virgocentric flow, yields a distance of 17.8 Mpc (for a Hubble constant of 70 km/s/Mpc). However, when the Tully-Fisher relation is used as distance indicator, the distance is found to be 6.5 Mpc (e.g. Hyperleda). For the higher distance, the gas to dynamical mass ratio is unrealistically high, favoring lower values. In the present work, we adopt the median value given by NED, i.e. D=10 Mpc, for which 1″ = 48 pc.

2. Observations

The observations were carried out on October 22, 2012 with the ALMA array in cycle 0, using 23 antennae, under the project ID 2011.0.00208.S (PI: Combes). NGC 1566 was observed with Band 7 simultaneously in CO(3-2), HCO^+(4-3), HCN(4-3), and continuum. The corresponding sky frequencies were 344.09 GHz, 354.98 GHz, 352.76 GHz, and 342.80 GHz, respectively. The observations were done in 2 blocks, with a total duration of 2 hours. For each period, NGC 1566 was observed for 28 minutes, and the median system temperatures were T_{sys} = 149 and 184 K.

The observations were centered on the nucleus, with a single-pointing field of view (FoV) equal to 18″; the extended configuration provided in Band 7 a beam of 0.64″x 0.43″, with a PA of 123°. The galaxy was observed in dual polarisation mode with 1.875 GHz total bandwidth per baseband, and velocity resolution of 0.49 MHz ∼0.4 km/s. The spectra were then smoothed to 11.7 MHz (10.15 km/s) to build channel maps.

The correlator configuration was constrained by the allowed spacing of the intermediate frequencies, and therefore the lines could not be centered in their bandwidths. Although the bandwidth provided almost 1600 km/s each, the lines were centered at 220-250 km/s from the edge for HCN and CO, and 440 km/s for HCO^+. Since the total line-width at zero intensity is less than 400 km/s, this constraint has no impact on the data. We stress that we cannot have missed any outflow similar to what have been already detected in the literature (for instance that in NGC 1266, Alatalo et al. 2011): these flows are roughly symmetric in velocity, and should appear complete on the side of full velocity coverage, and also as a truncated emission on the other side of the band, which we do not see.

The total integration time provided an rms of 0.05 mJy/beam in the continuum, and ∼1.3 mJy/beam in the line cubes at

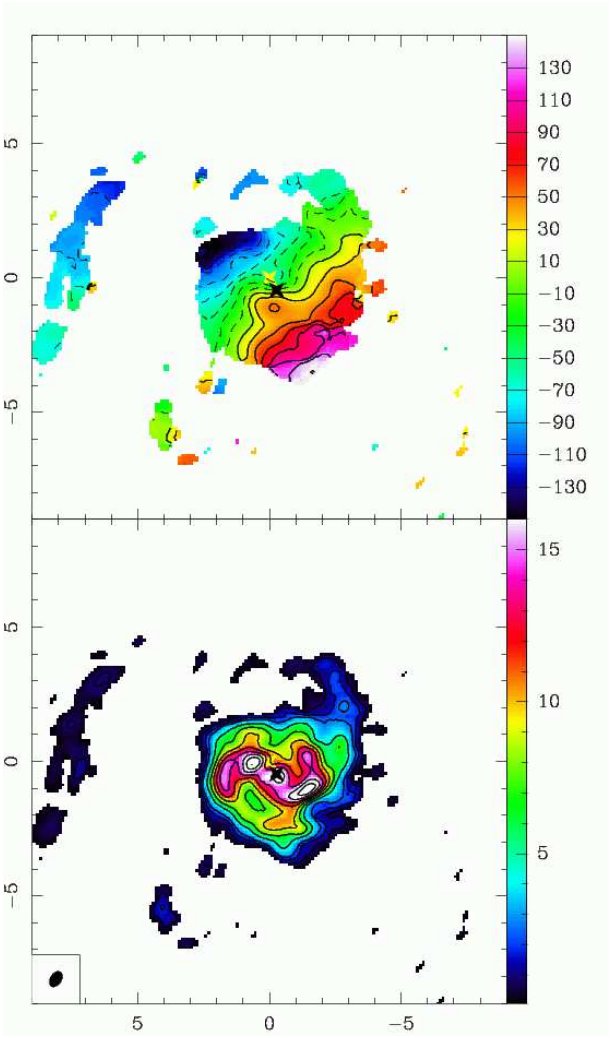

Fig. 3. Velocity field (top) and integrated intensity (bottom) of the CO(3-2) emission in the center of NGC 1566. Coordinates are in arcsec relative to the phase center of Table 1. The latter is indicated as a yellow cross, and the new adopted center as a black cross (see Sec. 3.2). The color palettes are in km/s relative to V_{hel}=1504 km/s (top) and in Jy/beam×MHz (or 0.87 Jy/beam×km/s) at the bottom. The beam size of 0.64″ x 0.43″ is indicated at the bottom left.

Table 1. Basic data for the galaxy NGC 1566

Parameter	Value[b]	Reference[c]
α_{J2000}[a]	$04^h20^m00.42^s$	(1)
δ_{J2000}[a]	-54°56′16.1″	(1)
V_{hel}	1504 km s^{-1}	(1)
RC3 Type	SAB(s)bc	(1)
Nuclear Activity	Seyfert 1	(2)
Inclination	35.°0	(3)
Position Angle	44° ± 1°	(3)
Distance	10 Mpc (1″ = 48 pc)	(1)
L_B	8.8×10^9 L$_\odot$	(4)
M_{HI}	3.5×10^9 M$_\odot$	(5)
M_{H_2}	1.3×10^9 M$_\odot$	(6)
M_{dust}(60 and 100 μm)	3.7×10^6 M$_\odot$	(7)
L_{FIR}	6.5×10^9 L$_\odot$	(7)
M_{BH}	8.3×10^6 M$_\odot$	(2)
L_{bol}	1.0×10^{44} erg/s	(2)
α_{J2000}[d]	$04^h20^m00.39^s$	New center
δ_{J2000}[d]	-54°56′16.6″	New center

[a] (α_{J2000}, δ_{J2000}) is the phase tracking center of our ^{12}CO interferometric observations.
[b] Luminosity and mass values extracted from the literature have been scaled to the distance of D = 10 Mpc.
[c] References: (1) NASA/IPAC Extragalactic Database (NED, http://nedwww.ipac.caltech.edu/); (2) Woo & Urry (2002); (3) Agüero et al. (2004); (4) HyperLeda; (5) Reif et al. (1982); (6) Bajaja et al. (1995); (7) IRAS Catalog.
[d] New adopted center, coinciding with the continuum peak (see Sec. 3.2).

Table 2. Line fluxes, after primary beam correction.

Line	Area	V	$\Delta V^{(1)}$	Flux$^{(2)}$
	Jy km/s	km/s	km/s	Jy
CO(3-2)	596± 2	1516±0.3	155± 1	3.6
C1	21± 1	1368±1	42± 1	0.5
C2	197± 5	1455±1	77± 1	2.4
C3	368± 5	1545±1	91± 1	3.8
HCO^+(4-3)	5.7± 0.6	1509±7	135± 14	0.04
HCN(4-3)	1.8± 0.4	1540±7	57± 14	0.03

Results of the Gaussian fits: first line for CO(3-2) assumes only one component; following lines assume 3 velocity components (C1, C2 and C3), shown in Fig. 10.
(1) Full width at half maximum (FWHM)
(2) Peak flux

10 km/s resolution. Flux calibration was done on Neptune, after subtracting the line contribution from its spectrum; bandpass calibration used J1924-292, and the phase calibrations the nearby radio source J0455-462.

The maps were made with Briggs weighting and a robustness parameter of 0.5, i.e. a trade-off between uniform and natural weighting. The data were cleaned using a mask made from the integrated CO(3-2) map. The continuum was subtracted from all line maps. The final cubes are 256x256 pixels of 0.11″ per pixel in the plane of the sky, and 50 channels of ∼10 km/s width. The data were calibrated with the CASA software (v4.1; McMullin et al. 2007), and the cleaning and imaging were then finalised with the GILDAS software (Guilloteau & Lucas 2000).

The maps and images shown in the figures of the present paper are not corrected for primary beam attenuation. However, the integrated spectra include primary beam correction, and the total masses are computed with the correction applied. Almost no CO(3-2) emission was detected outside the full width at half-power (FWHP) primary beam. Due to missing short spacings, extended emission was filtered out at scales larger than ∼3″ in each channel map. The elongated features detected at each velocity are, however, quite narrow spatially, thinner than 2″, and the loss of flux may not be severe at any velocity, as can be seen in Fig. 2.

3. Results

Figure 2 displays 42 of the CO(3-2) channel maps, with a velocity range of 416 km/s and a velocity resolution of 10.15 km/s. The velocity field is rather regular, showing the expected spider diagram, although slightly perturbed by spiral structure in the SE and NW directions (see also Fig. 3).

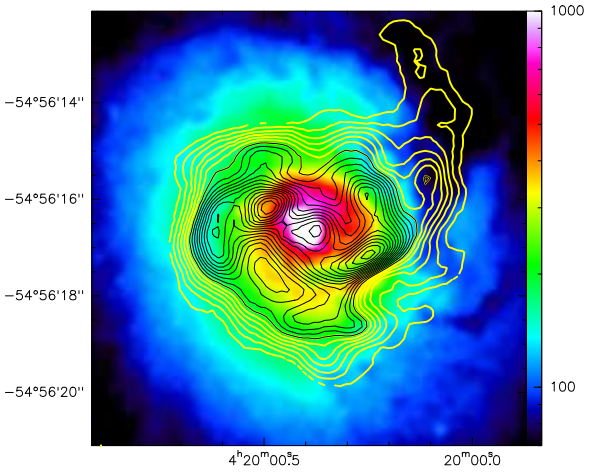

Fig. 4. Overlay of CO(3-2) contours on the (F606W) HST image. The colour scale is linear, in arbitrary units. Notice the perfect coincidence between the emergent spiral arm in CO(3-2) and the dust extinction in the NW. CO contours are linear from 0.04 to 17.44 in steps of 0.87 Jy/beam.km/s. The first contours of the CO(3-2) emission are drawn in yellow to be visible against the dark dust lane.

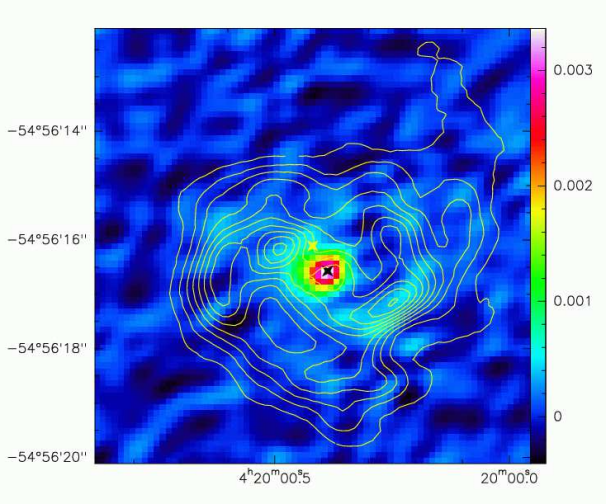

Fig. 5. Overlay of CO(3-2) contours (as in Fig. 4) on the 0.87mm continuum image. The field of view is 8″ in diameter. The yellow cross shows the phase center, while the black cross defines the new center adopted in Table 1. The colour scale is in Jy/beam.

3.1. Molecular gas distribution and morphology

To measure fluxes we used a clipped cube where all pixel values <2σ (2.6 mJy/beam) were set to zero. The mean intensity is plotted in the lower panel of Fig. 3. Since the galaxy is more extended than the primary beam of 18″, it is difficult to quantify the missing flux. We compare with the central spectrum obtained with a single dish in Sect. 3.4, and conclude that we might miss roughly half of the total. These single dish observations were obtained with the SEST in CO(2-1) with a 22″ beam. The angular size is comparable to our FoV, but assumptions have to be made about the CO line ratios.

The CO emission is concentrated in a nuclear disk of radius 3″or 150 pc, where it shows a contrasted 2-arm spiral structure. The molecular gas does not seem to follow the nuclear bar. This spiral structure at a ~ 100 pc scale appears independent from the large-scale grand design 2-arm structure, starting at its pseudo-nuclear ring of ~ 35″=1.7 kpc in radius (Elmegreen & Elmegreen 1990). We superposed the CO map onto HST images in the U, B, V and I filters (F275W, F450W, F606W, F814W). All show a remarkable similarity in morphology, with the dust extinction features progressively less contrasted, as displayed in Figure 4. The CO emission in the open spiral arms nicely corresponds to the dust lanes.

These two small spiral arms show a faint extension with a progressively smaller pitch angle, winding up onto a pseudo-ring of radius ~ 9″=430 pc. The ring is at the edge of the FoV, and is therefore stronger in reality than it appears in our map. This ring might correspond to the inner Lindblad resonance of the nu-

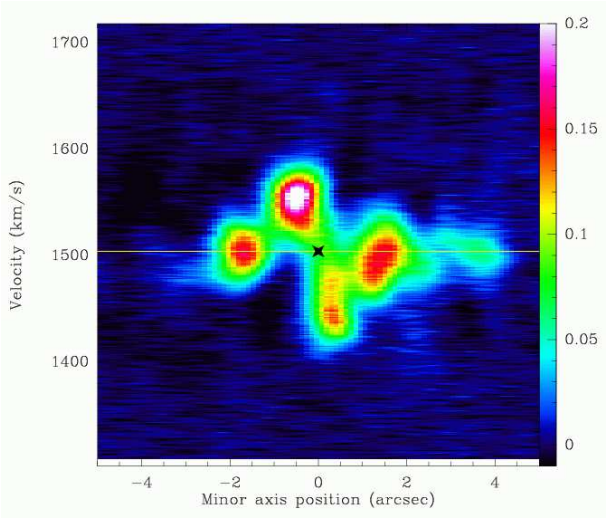

Fig. 6. CO(3-2) position-velocity diagram along the minor axis at PA = 134° (SE is at left, and is the far side). Note the small deviations from a constant radial velocity, which come from spiral streaming motions. The black cross indicates the adopted center.

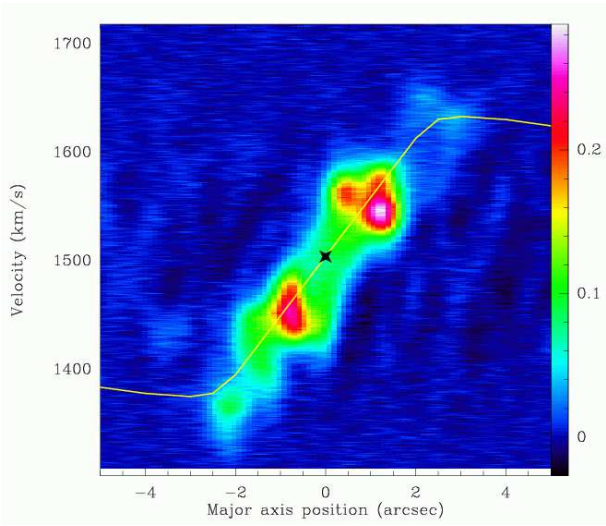

Fig. 7. CO(3-2) position-velocity diagram along the major axis at PA = 44° (East is at left). The velocity profile is quite regular, and matches with the expected rotational velocity gradient (yellow line), as modelled in Fig. 9. The black cross indicates the adopted center.

clear bar (e.g. Buta & Combes 1996). Such a ring has also been identified by Comeron et al. (2010) at 9.7″=465 pc radius from the HST images, and corresponds to weak star forming regions in ionised gas (Comte & Duquennoy 1982; Agüero et al. 2004). The main star-forming ring is, however, at the end of the bar, at about 1.5 kpc (Elmegreen & Elmegreen 1990).

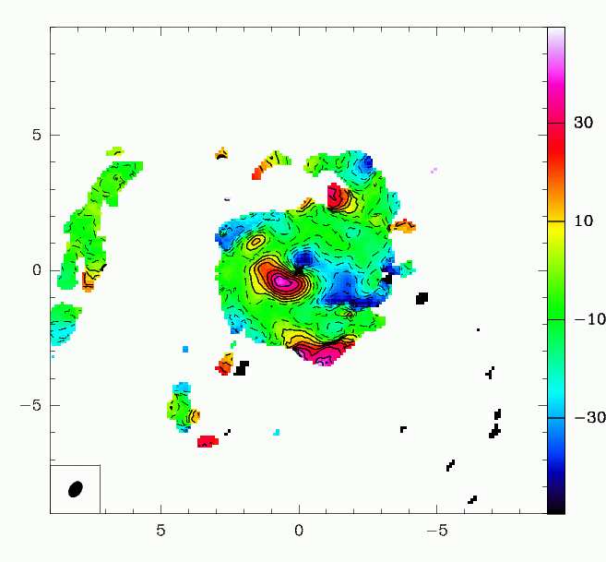

Fig. 8. Velocity residuals after subtraction of a regular rotation model, based on the CO data, as displayed in Figure 9. The beam size of 0.64″ x 0.43″ (30 x 20 pc) is indicated at lower left. The black cross indicates the adopted center.

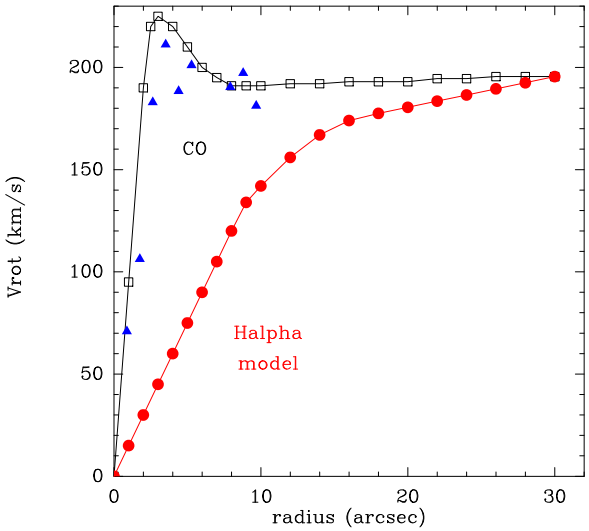

Fig. 9. Rotational velocity model adopted for NGC 1566 (black open rectangles), based on the CO data points (blue triangles), and minimizing the residuals of Fig. 8. The Hα kinematic model from Agüero et al. (2004) is also shown in red circles. Those data were obtained with 2.″8-wide slits, with insufficient spatial resolution to resolve the central peak. The Hα velocity model rises linearly because of the deficiency of HII regions inside a radius of 22″ (see text).

3.2. Continuum emission

Continuum emission was detected at 0.87mm, using all four sub-bands, once the lines were subtracted. The bandwidth available then amounts to 6500 MHz, yielding an rms noise level of 0.055 mJy. Fig. 5 displays the CO(3-2) contours superposed on the continuum map. The ~ 3mJy peak emission is detected at 50σ significance. The emission is extended, and follows the 2-arm spiral structure already detected in the CO(3-2) line. The dust emission has already been detected at many wavelengths in this galaxy, with IRAS, ISO and *Spitzer*. It peaks at 102 Jy at 160μm (Dale et al. 2007), and is still 9.1 Jy at 500μm (Wiebe et al. 2009). The emission we see at 870μm is thus expected to come essentially from dust. From the radio emission at cm wavelengths, the slope of the synchrotron emission can be derived to be -0.8. Extrapolating from the measured point at 5 GHz, the total synchrotron emission is expected to be 3mJy. On the high frequency side, the extrapolation of a grey-body, with a dust opacity $\propto \nu^2$, gives a flux at 870 microns of 1 Jy. The dust emission is then dominating the flux at 870 microns.

The total continuum emission integrated over our FoV amounts to 12.5 mJy, which is consistent with the extrapolation of the far-infrared SED from previous measurements, if account is taken for the missing flux and the continuum extent: the total flux for the whole galaxy should be of the order of 1 Jy. Most of the emission must come from outside the ALMA FoV, and it is likely that the interferometer misses a significant part of the emission, more so than for the line where the velocity splitting reduces the extent of the emission, in each channel.

The central peak in the continuum emission, coinciding with the peak in the CO(3-2) emission at the center of the nuclear spiral arm, is adopted as the new center of the galaxy (cf Table 1). The distance between the two centers is ~ 0.5″ = 24 pc, and might result from the uncertainty of the optical position because of dust patches at the center.

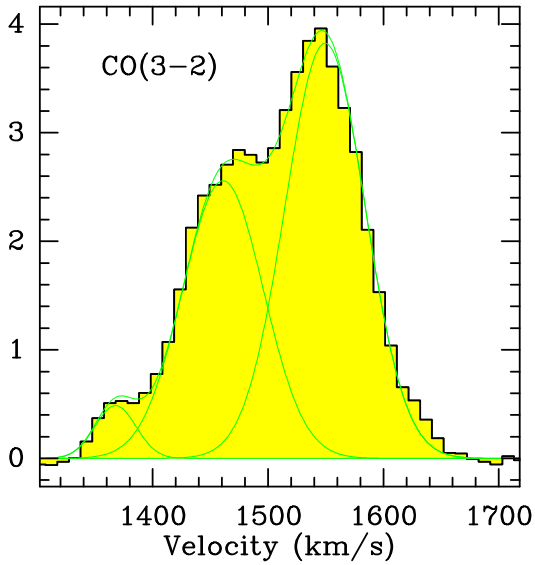

Fig. 10. Total CO(3-2) spectrum, integrated over the observed map, with a FoV of 18″. The vertical scale is in Jy. The green line is the result of the gaussian fit with 3 velocity components (see Table 2). The spectrum is primary beam corrected.

3.3. CO kinematics

The top panel of Figure 3 displays the velocity field of the molecular gas. The velocity field is well described by rotation, with the major axis at a position angle of 44° and an inclination of 35° as determined by optical studies at larger scales. The CO velocities reveal a peak in the rotation curve at about 2″, then a slight decrease to reach a plateau, similar to what is found in optical studies. Although the CO rotation curve shown in Fig. 9 seems to be poorly constrained by the scattered CO data points, it was more precisely derived by minimising the residuals in the 2D map (see below).

The Hα rotation curve was determined by Agüero et al. (2004) from 6 slits of width 2.″8 that have insufficient spatial resolution to resolve the 2″ peak. In addition, there is a deficiency of HII regions inside a radius of 22″= 1 kpc, corresponding to the pseudo ring where the grand design spiral arms begin. The Fabry-Perot Hα rotation curves from Comte & Duquennoy (1982) and Pence et al. (1990) also suffer from this HII region deficiency, and are consistent with our curve only at larger radii. The model Hα rotation curve from Agüero et al. (2004) shown in Fig. 9 follows a linear curve inside the ring, as expected for any tracer distribution with a hole at the center. The main star forming ring appears at the end of the bar, and might correspond to the corotation of the bar, coinciding with the inner Lindblad resonance of the spiral (Elmegreen & Elmegreen 1990). This would explain the deficiency of ionised gas inside 1 kpc radius. Therefore, only the CO gas can probe the disk inside the stellar bar. The deficiency of star formation in these regions emitting molecular lines might be due to the dynamical state of the gas, which disfavors star formation, like in NGC 1530 for example (Reynaud & Downes 1998).

The stellar bar is mainly visible in red and near-infrared images, inside the star forming ring. The molecular gas does not follow the bar, but instead develops a nuclear spiral structure, which reflects some kinematical perturbations. These are most visible in the position-velocity diagram along the minor axis (Fig. 6), while the rotation is more regular along the major axis (Fig. 7). These kinematic disturbances arise more from gaseous spiral and turbulent perturbations than from coherent streaming motions due to a bar. This situation is similar to that in other galaxies in the NUGA sample, which show similar wiggles on the minor axis PV diagram but remain regular on the major axis: NGC 4826 (García-Burillo et al. 2003), NGC 3147 (Casasola et al. 2008) or NGC 1961 (Combes et al. 2009). In NGC 1566, the bar has a position angle of nearly 0°, significantly different from the major axis position angle of 44°. This is a favorable situation for measuring streaming motions due to the bar. However, the gas follows its own spiral structure that is more aligned with the major axis, explaining why little perturbation shows up along this symmetry axis.

Another way to reveal peculiar velocities in 2D over the nuclear region is to subtract the expected regular velocity field derived from the CO data from the velocity field. Fig. 8 displays the residuals obtained relative to the adopted rotation curve model of Fig. 9. They are very low all over the map, and peak at ~ 30 km/s S-SE of the nucleus, corresponding to the edge of an arm. Since at large-scale trailing spiral structures are always dominant, the observed velocity field indicates that the SE region is the far side, and the NW the near side. Streaming motions are stronger on the far side, but are present on both sides, while following the spiral arms. This pattern is not characteristic of a symmetric outflow of gas. It has the right sign for an outflow, since it is redshifted on the far side of the minor axis and blueshifted on the near side, but it has much too small an amplitude. Note also that at larger scales, Agüero et al. (2004) find the opposite, i.e. an inflow of gas along the minor axis (see their Fig 3), with a comparable amplitude. This supports our interpretation in terms of streaming motions. The stronger "outflow" feature coincides in size and position with the one-sided NLR ionised cone in the [OIII] high resolution image of Schmitt & Kinney (1996), but the coincidence is most likely spurious, since there is no reason for the cone to be related to the spiral arm streaming motion.

3.4. H_2 mass

Figure 10 displays the total CO(3-2) spectrum integrated over the observed map. When integrated over the spectral range (FWHM=155km/s), the integrated emission is 596± 2 Jy km/s. Towards the central position, Bajaja et al. (1995) found a CO(2-1) spectrum peaking at T_A^*= 120mK with FWHM=200 km/s, yielding a total integrated flux of 660 Jy km/s, in a beam of 22″. Since their beam is very similar to our FoV, the comparison is meaningful, telling us that we are certainly missing some flux, by a factor up to ~ 2. Indeed, the CO excitation appears high at the center of NGC 1566, since the CO(2-1)/CO(1-0) intensity ratio is about 1 in temperature units, averaged over the 43″ beam (Bajaja et al. 1995). This is expected for thermalized excitation and a dense molecular medium. In that case the CO(3-2) flux should be higher than the CO(2-1) by up to a factor of 2.2 (flux varying as $\sim \nu^2$ for gas at temperature larger than 25K and density larger than 10^4 cm^{-3}). Already the CO(2-1) spectrum of Bajaja et al. (1995) appears broader in velocity, which indicates some missing flux in our CO(3-2) map. The SEST observations point to a total molecular mass of 1.3 10^9 $M_\odot$, and in the central 43″ beam of 3.5 10^8 $M_\odot$. In the 22″ beam, the SEST CO(2-1) spectrum, together with the CO(2-1)/CO(1-0) ratio of 1, yields a mass 1.7×10^8 $M_\odot$, while we find 0.7×10^8 $M_\odot$ in our FoV of 18″ assuming thermally excited gas, and a Milky-Way like CO-to-H_2 conversion factor, of 2.3 10^{20}cm^{-2}/(Kkm/s) (e.g. Solomon & Vanden Bout 2005).

3.5. HCO^+ and HCN

Along with CO(3-2), we detect the HCO^+(4-3) and HCN(4-3) emission lines, mainly in the center of the galaxy. The corresponding maps are displayed in Figure 11, and the integrated spectra in Figure 12. The lines are mainly detected in the nuclear spiral structure, and are too faint to see the rest of the nuclear disk. The HCO^+ line is 3 times stronger than the HCN line, which is expected for starburst galaxies such as M82 (e. g. Seaquist & Frayer 2000). The detection of these lines reveals a high proportion of dense gas, since the critical densities to excite the J=4-3 transition of HCO^+ and HCN are 6.5 10^6 and 1.6 10^8 cm^{-3}, respectively.

The integrated intensities and profile characteristics displayed in Table 2 reveal that the HCO^+ line width is comparable to the CO(3-2) width, while the HCN spectrum appears truncated, as if only one side of the galaxy, the redshifted SW part, is strong enough to be detected. The total intensities of both lines are, however, weak: HCO^+(4-3) is 100 times weaker than CO(3-2), and HCN(4-3) is 300 times weaker than CO(3-2). These ratios are about 3 times less than at the center of M82, and suggest a lower fraction of dense gas (e.g. Naylor et al. 2010). This is expected since NGC 1566 is not a starburst galaxy (e.g., Gao & Solomon 2004).

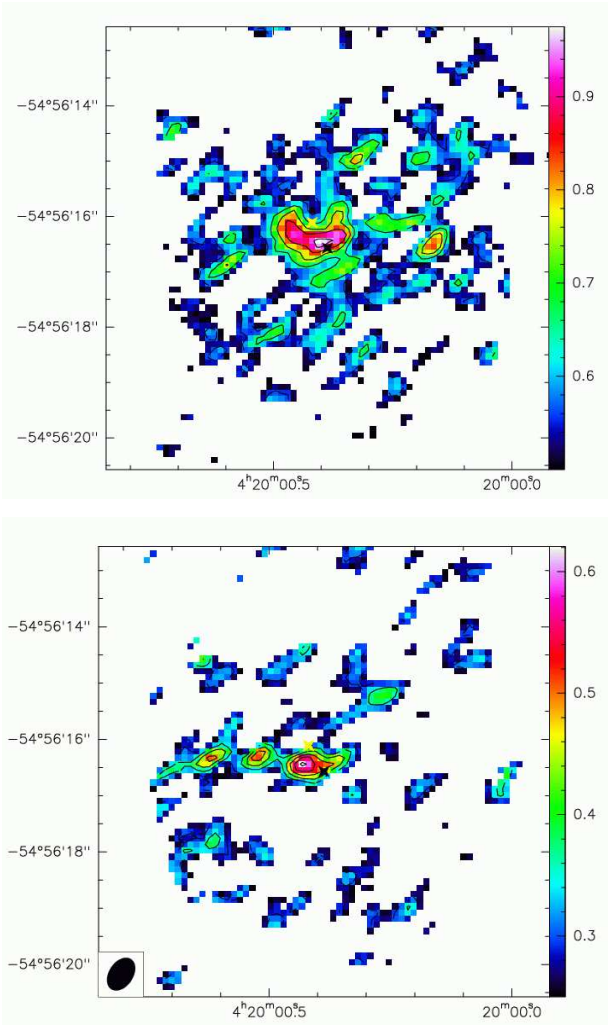

Fig. 11. *Top*: Map of the HCO^+(4-3) line in NGC 1566. The adopted center is drawn with a black cross, and the phase center by a yellow cross. The color scale is in Jy/beam×MHz (or 0.87 Jy/beam×km/s). *Bottom:* Same for HCN(4-3). The beam size of 30 x 20 pc is indicated at the lower left.

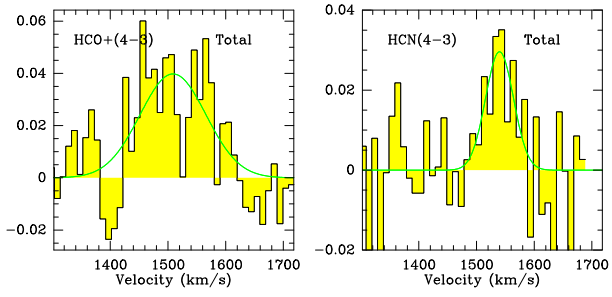

Fig. 12. Total HCO^+(4-3)*(left)* and HCN(4-3) *(right)* spectra, integrated over the field of view of 18″, after primary beam correction. The vertical scale is in Jy. The green lines are the Gaussian fits, whose parameters are displayed in Table 2.

The fact that the HCO^+ emission is 3 times stronger than the HCN emission indicates that the excitation of the molecules at the center of NGC 1566 is dominated by star formation (PDR or photodissociation region), and not the AGN (XDR or X-ray dominated region). Indeed, in AGN-dominated molecular disks, the HCN/HCO^+ ratio can reach values much larger than 1 (Kohno et al. 2003; Krips et al. 2008; García-Burillo et al. 2010; Costagliola et al. 2011; Imanishi & Nakanishi 2013).

4. Torques and AGN fueling

A small bar is detected in red and near-infrared images of NGC 1566 (see for example Fig. 1 from Agüero et al. 2004, from 2MASS). Its position angle is PA=0°, and its length is 35″= 1.7 kpc, as determined by Hackwell & Schweizer (1983), or Comeron et al. (2010). According to Elmegreen & Elmegreen (1990), this radius coincides with kinks in the spiral arms, and the amplitude of the conspicuous 2-arm grand design spiral begins to increase. We have used a red image (F814W) from HST to derive the stellar potential in the center, since 2MASS images have insufficient angular resolution. We have not separated the bulge from the disk contribution since NGC 1566 is a late type (Sbc) galaxy. This means that the bulge was effectively assumed to be flattened. Dark matter can be safely neglected inside the central kpc. The image has been rotated and deprojected according to PA=44° and i=35°, and then Fourier transformed to compute the gravitational potential and forces. A stellar exponential disk thickness of ~1/12th of the radial scale-length of the galaxy (h_r=3.8kpc) has been assumed, giving h_z=317pc. This is the average scale ratio for galaxies of this type (e.g., Barteldrees & Dettmar 1994; Bizyaev & Mitronova 2002, 2009). The potential has been obtained assuming a constant mass-to-light ratio of M/L = 0.5 $M_\odot/L_\odot$ in the I-band over the considered portion of the image of 2 kpc in size. This value is realistic in view of what is found statistically for spiral galaxies (Bell & de Jong 2001). The pixel size of the map is 0.079″=3.8 pc. The stellar M/L value was fit to reproduce the observed CO rotation curve. We have checked that the results are not significantly changed when the geometrical parameters (i and PA) are varied by ±5°, as found in the literature. The M/L varies as 1/sin^{2}i accordingly.

The potential $\Phi(R,\theta)$ can be decomposed into its different Fourier components:

$$\Phi(R,\theta) = \Phi_0(R) + \sum_m \Phi_m(R)\cos(m\theta - \phi_m(R))$$

The strength of the m-Fourier component, $Q_m(R)$ is defined as $Q_m(R) = m\Phi_m/R|F_0(R)|$, i.e. by the ratio between tangential and radial forces (e.g. Combes & Sanders 1981). The strength of the total non-axisymmetric perturbation $Q_T(R)$ is defined similarly with the maximum amplitude of the tangential force $F_T^{max}(R)$. Their radial distributions and the radial phase variations are displayed in Fig. 13.

The derivatives of the potential yield the forces per unit mass (F_x and F_y) at each pixel, and the torques per unit mass $t(x,y)$ are then computed by:

$$t(x,y) = x\,F_y - y\,F_x$$

The sign of the torque is determined relative to the sense of rotation in the plane of the galaxy. The product of the torque and the gas density Σ at each pixel allows one then to derive the net effect on the gas, at each radius. This quantity $t(x,y)\times\Sigma(x,y)$, is shown in Fig. 14.

The torque weighted by the gas density $\Sigma(x,y)$ is then averaged over azimuth, i.e.

$$t(R) = \frac{\int_\theta \Sigma(x,y)\times(x\,F_y - y\,F_x)}{\int_\theta \Sigma(x,y)}$$

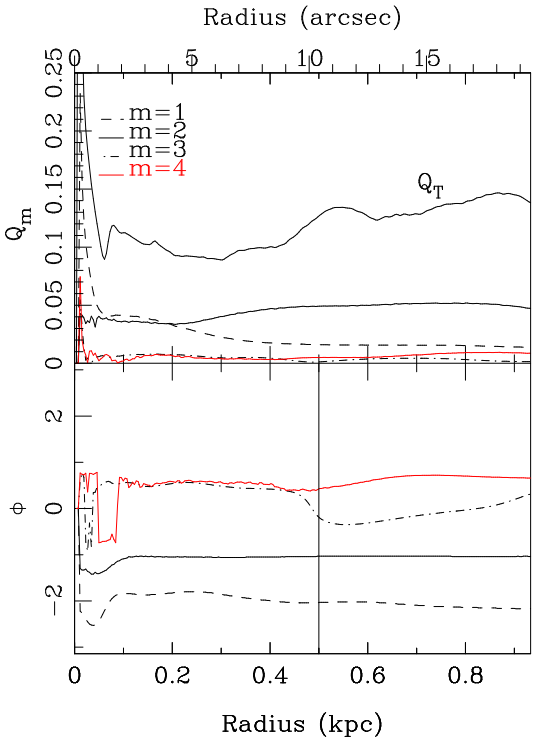

Fig. 13. *Top* Strengths (Q_m and total Q_T) of the $m = 1$ to $m = 4$ Fourier components of the stellar potential within the central kpc. The $m = 2$ term is dominant, and has a constant phase, corresponding to the bar. *Bottom* Corresponding phases in radians of the Fourier components, taken from the major axis, in the deprojected image. The vertical line indicates the proposed ILR position for the nuclear bar.

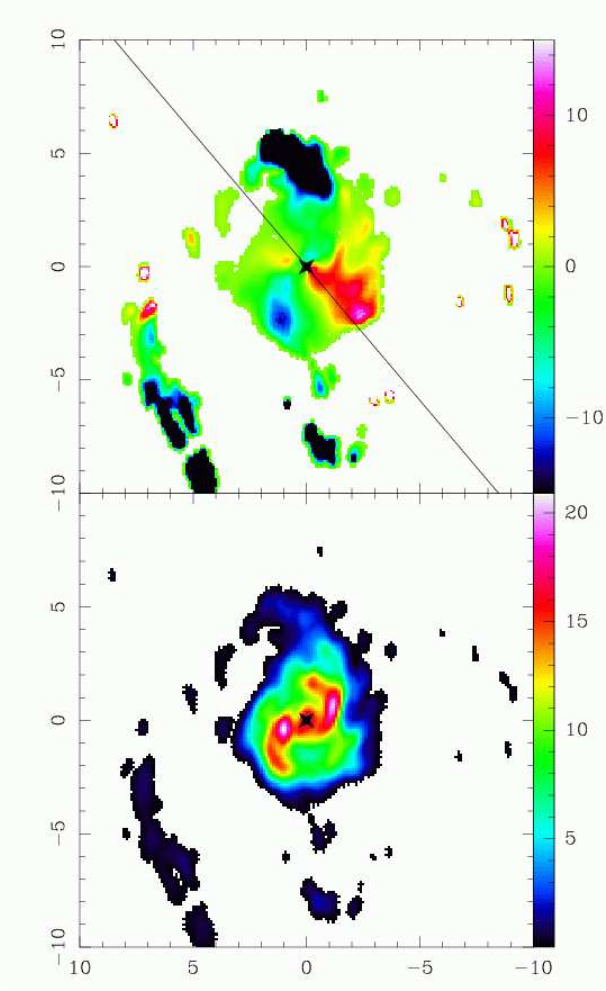

Fig. 14. *Top:* Map of the gravitational torque, (t(x,y) × Σ(x,y), as defined in text) in the center of NGC 1566. The torques change sign as expected in a four-quadrant pattern (or butterfly diagram). The orientation of the quadrants follows the nuclear bar's orientation. In this deprojected picture, the major axis of the galaxy is oriented parallel to the horizontal axis. The inclined line reproduces the mean orientation of the bar (PA = 40° on the deprojected image). *Bottom:* The deprojected image of the CO(3-2) emission, at the same scale, and with the same orientation, for comparison. The axes are labelled in arcsecond relative to the center. The color scales are linear, in arbitrary units.

The quantity $t(R)$ represents the time derivative of the specific angular momentum L of the gas averaged azimuthally (e.g. García-Burillo et al. 2005). Normalising at each radius by the angular momentum and rotation period allows us to estimate the efficiency of the gas flow, as shown in Fig. 15.

Although the nuclear bar strength is moderate, Fig. 15 shows that its fueling efficiency is high. Between 200 and 300 pc, the gas loses half of its angular momentum in one rotation, which is ∼ 7 Myr. Inside 100 pc, the relative loss rate is lower, but other dynamical phenomena can then contribute, such as dynamical friction of molecular clouds against the distribution of stars. The rotation period becomes smaller than 3Myr, and the dynamical friction time-scale is decreasing rapidly, especially for massive giant molecular clouds. Since dense clouds exist at the center of NGC 1566, as supported by the HCN and HCO^+ detections, this might be the mechanism for driving the gas down to 10 pc scales, in times comparable to a few rotation periods. The dynamical friction time-scale t_{df} at a radius R can be estimated in a galaxy like the Milky Way as t_{df} (Myr) = $(R/10pc)^2$ $(10^6\ M_\odot/M_{cloud})$ for a molecular cloud of mass M_{cloud} (e.g., Combes 2002).

As shown in Fig. 14, the nuclear spiral structure inside the nuclear ILR ring of the bar is of a trailing nature and is located inside the negative torque quadrants. This might appear suprising, since in many cases the spiral structure is predicted to be leading in this region, and the torque positive, maintaining the gas in the ILR ring (e.g., Buta & Combes 1996). However, in the presence of a sufficiently massive black hole, this behaviour can be reversed: the spiral becomes trailing, and the torque negative. Indeed, the indicator of the precession rate of elliptical orbits in the frame of the epicyclic approximation, $\Omega - \kappa/2$, is significantly modified by a central massive body. Instead of decreasing regularly towards zero at the center, the $\Omega - \kappa/2$ curve increases steeply as $r^{-3/2}$. The gas undergoes collisions, loses energy and spirals progressively towards the center. When the precession rate decreases, the series of elliptical orbits precess more and more slowly, and then lag at smaller radii, forming a leading structure. When the precession rate increases, they form a trailing structure.

Another question is whether the orbits change orientation at the ILR, as expected if the x_2 orbits develop between two inner resonances. This would destroy the nuclear bar and be observable on the infrared image. The lower panel of Fig. 13 shows the phases of the various Fourier components. The bar ($m = 2$) has a constant phase over its length, and their orientation change does not appear to be significant.

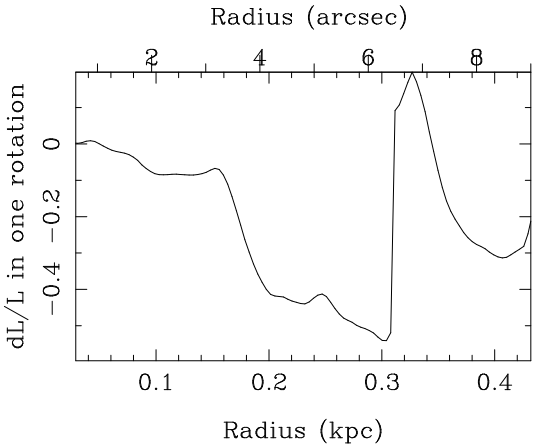

Fig. 15. The radial distribution of the torque, quantified by the fraction of the angular momentum transferred from the gas in one rotation–dL/L, estimated from the CO(3-2) deprojected map. The forces at each point of the map were computed from the I-band HST image (see text). The torque is negative inside a 0.3 kpc radius and down to the spatial resolution of the observations. Between 6 and 9″ from the center, there is not much CO emission and the torque estimation is noisy.

NGC 1566 is therefore an example of a trailing spiral inside the nuclear ring of a bar i.e., the case described in Fig 79b of Buta & Combes (1996). This means that the mass of the black hole should be sufficiently high to have an influence on the gas dynamics on a 100 pc scale. Woo & Urry (2002) have estimated a BH mass of M_{BH} = 8.3 10^6 $M_\odot$ from the M-σ relation using a measured central velocity dispersion (Table 1). With this plausible black hole mass, we have estimated the BH influence. Although the modification of the rotation curve is very small, the influence on the precession rate $\Omega - \kappa/2$ is more significant. Figure 16 illustrates more clearly how this is possible.

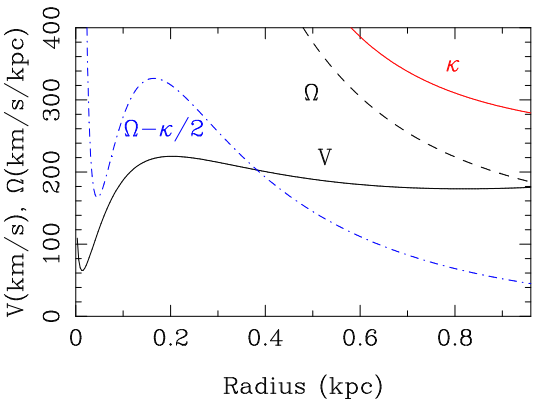

Fig. 16. Schematic representation of the rotation curve (black) epicyclic frequency κ (red), and corresponding $\Omega - \kappa/2$ curve (blue) within the central kpc of NGC 1566. The contribution of a super-massive black hole in the nucleus with M_{BH} = 8.3 10^6 $M_\odot$ has been included.

In this figure, we selected an analytical form for the rotation curve that schematically reproduces the observed one. It is not possible to make a better fit, given that only the CO emission is able to trace the kinematics in this region. If we locate corotation at the end of the bar, i.e. at a radius of 1.7 kpc, then the pattern speed of the bar is ∼ 120 km/s/kpc. The ILR is then approximately at a radius of 500 pc, near the location where we found the resonant ring (see Sec. 3.1 and also Comeron et al. 2010). This is a good fit, given that the computation of resonances via the $\Omega - \kappa/2$ curve and the epicyclic approximation is not accurate. The precession rate of the infalling orbits is then going to increase towards the center, accounting for the trailing spiral structure observed.

Fig. 16 shows that the influence of the black hole on the rotation curve is almost negligible; it is significant only inside 13 pc. However, it is more important in influencing the precession rate, which includes the second derivative of Ω. The influence of the BH is then felt up to 50 pc. Since the 100 pc-scale arms are defined by elongated orbits extending below 50 pc, it is possible that the black hole indeed has an influence on the 2-arm spiral structure inside the ILR ring.

4.1. Comparison with other nuclear patterns

The observation of a trailing 2-arm spiral structure inside the ILR of a nuclear bar is a rare configuration. In molecular gas morphologies, this case had not previously been encountered. Although previous NUGA studies have not had the advantage of as small a physical resolution as the current ALMA data, it is useful to make some statistical considerations. Looking at previous NUGA galaxies where detailed torques have been measured, it is possible to distinguish at least three generic configurations (see also García-Burillo & Combes 2012):

1. There is no ILR, and the trailing structure goes right to the nucleus from corotation (CR). A trailing spiral structure is then expected throughout, with negative torques (as in NGC 3147, 3627). In some cases, like NGC 6574, there is an ILR, but it cannot be resolved with the CO beam; negative torques are measured from CR to ILR. So this case is also similar to the no-ILR case.
2. There is an ILR, and a ring or pseudo-ring at the ILR, which is resolved by the molecular observations. The molecular gas reveals a hole inside the ring, or is highly deficient inside that radius. The torque is positive inside the ILR (negative outside), so the gas is piling up in the ring. When there is some CO emission inside the ring, its distribution is in general patchy, with no clear arms; it could be a mixture of leading and trailing features, but there must be some leading pattern to account for positive torques (this is the case for NGC 4321, 4569, 5248, 5953, 6951 and 7217). NGC 1433 is also in this configuration, although the nuclear spiral structure is rather flocculent (Combes et al. 2013). The spiral is trailing between CR and ILR of the nuclear bar, and within the ILR at 200 pc in radius, the spiral structure is unclear, but the torque is positive.
3. There is an independent embedded structure, a nuclear bar with a different pattern speed from that of the primary bar, and a negative torque can be measured inside the CR of the nuclear bar, but without a coherent orientation (case of NGC 2782).

There are also other special cases, e.g. involving development of a dominant $m = 1$ pattern in the center, like NGC 1961, 4826, or 5850.

Another way to detect spiral structure in the nuclear gas is to amplify the dust extinction features in the HST images through unsharp masking. Martini et al. (2003a,b) have studied the presence of circumnuclear dust in 123 galaxies, of which 14 have

nuclear rings. When circumnuclear dust features are present, they have classified them as grand design 2-arm structures (GD), multi-arm or floculent structures (tightly or loosely wound) and chaotic structures (spiral or not). Only 19 galaxies have GD nuclear morphologies, and among the nuclear ring galaxies, only 3 are classified as GD (NGC 1300, 3081 and 6890). Only galaxies with large scale bars exhibit GD nuclear spiral structure. Most of these spiral structures continue the dust lanes along the bar, without any ILR. In their sample of 75 nearby galaxies, Peeples & Martini (2006) find 7 objects with GD nuclear spirals. Only two have both a large-scale grand design and a GD, NGC 3081 and 5643. In these galaxies, however, the sense of winding of the dust spirals in the very center is unclear, and there could be a mixture of leading and trailing features. A clear case of a trailing spiral inside a nuclear ring is still missing. We have also examined the compilation of nuclear rings of Comeron et al. (2010). Most rings are either devoid of structure, or display confused or chaotic dust structures. Although the nuclear ring is clearly seen in the NGC 1566 image, the interior structure is difficult to distinguish in dust maps, making the molecular gas emission a better tracer.

5. Summary

We have presented ALMA cycle 0 results for a Seyfert 1 galaxy from our extended NUGA sample, NGC 1566. The observations in CO(3-2) allow us to reach a superb spatial resolution of 25 pc, even in this early cycle.

The center of NGC 1566 has a dense nuclear disk of molecular gas, that is deficient in both atomic gas and HII regions. The central disk is typically $\sim 3.5''$=170 pc in radius, and reveals an open 2-arm nuclear spiral structure, which tends to wind up into a faint ring at 430 pc radius. The spiral structure coincides very well with obscured dust lanes in HST images, and also with dust continuum emission at 870μm. The nuclear spiral arms are dense enough to be detected in the HCO^+(4-3) and HCN(4-3) lines.

The kinematics of the CO emission show a rather regular rotational velocity field, with only slight perturbations from the 2-arm nuclear spiral. There are in particular redshifted streaming motions on the SE part of the minor axis, and blueshifted ones on the NW side, along the border of the spiral arms. However, the amplitude of these perturbations is small, and it is remarkable that no symmetric molecular outflow, indicating a possible AGN feedback, is observed.

The faint CO ring at r=430 pc, which is more strongly noticeable in the V-I colour HST image (Comeron et al. 2010), is plausibly stronger in reality given the reduced sensitivity at the edge of our FoV. This ring corresponds to the ILR of the bar, if corotation is assumed to coincide with the bar end. The trailing spiral observed in CO emission is then well inside the ILR ring of the bar. We have computed the gravitational potential from the stars within the central kpc, from the I-band HST image. Weighting the torques on each pixel by the gas surface density observed in the CO(3-2) line has allowed us to estimate the sense of the angular momentum exchange and its efficiency. The gravity torques are negative from 50 to 300pc. Between 200 pc and 300 pc, the gas loses half of its angular momentum in a rotation period. Gravity torques are then very efficient in fueling the AGN, and bring molecular clouds so close to the center that dynamical friction could drive them to the nucleus in a few Myr.

This work provides the first example of a clear trailing spiral observed in molecular gas inside the ILR ring of a bar, indicating that the super-massive black hole is influencing the gas dynamics significantly enough to reverse gravity torques. Instead of maintaining the ILR ring density, the torques are then driving the gas towards the nucleus, a first step towards possibly fueling the AGN.

Acknowledgements. The ALMA staff in Chile and ARC staff at IRAM are gratefully acknowledged for their help in the data reduction. We want to thank in particular Gaelle Dumas and Philippe Salomé for their useful advice. This paper makes use of the following ALMA data: ADS/JAO.ALMA#2011.0.00208.S. ALMA is a partnership of ESO (representing its member states), NSF (USA) and NINS (Japan), together with NRC (Canada) and NSC and ASIAA (Taiwan), in cooperation with the Republic of Chile. The Joint ALMA Observatory is operated by ESO, AUI/NRAO and NAOJ. The National Radio Astronomy Observatory is a facility of the National Science Foundation operated under cooperative agreement by Associated Universities, Inc. We used observations made with the NASA/ESA *Hubble* Space Telescope, and obtained from the *Hubble* Legacy Archive, which is a collaboration between the Space Telescope Science Institute (STScI/NASA), the Space Telescope European Coordinating Facility (ST-ECF/ESA), and the Canadian Astronomy Data Centre (CADC/NRC/CSA). F.C. acknowledges the European Research Council for the Advanced Grant Program Num 267399-Momentum. I.M. acknowledges financial support from the Spanish grant AYA2010-15169 and from the Junta de Andalucia through TIC-114 and the Excellence Project P08-TIC-03531. We made use of the NASA/IPAC Extragalactic Database (NED), and of the HyperLeda database.

References

Abramowicz, M. A., Xu, C., Lasota, J. P. 1986 IAU, S119, 371
Agüero E.L., Diaz R.J., Bajaja E., 2004, A&A 414, 453
Alatalo K., Blitz L., Young L.M. et al, 2011, ApJ 735, 88
Alloin, D., Pelat, D., Phillips, M. M., Whittle M., 1985 ApJ 288, 205
Alloin, D., Pelat, D., Phillips, M. M., Fosbury, R. A. E., Freeman, K., 1986 ApJ 308, 23
Bajaja E., Wielebinsli R., Reuter H.P. et al. , 1995, A&AS 114, 147
Baribaud, T., Alloin, D., Glass, I., Pelat, D., 1992 A&A 256, 375
Barteldrees A., Dettmar R-J., 1994 A&AS 103, 475
Bell E.F., de Jong R.S., 2001, ApJ 550, 212
Buta R., Combes F., 1996, Fal of Cosmics Physics 17, 95
Bizyaev, D., Mitronova, S. 2002, A&A, 389, 795
Bizyaev, D., Mitronova, S. 2009, ApJ 702, 1567
Casasola, V., Combes, F., Garca-Burillo, S. et al. , 2008, A&A 490, 61
Comeron, S., Knapen, J. H., Beckman, J. E. et al. , 2010, MNRAS 402, 2462
Combes F., Sanders R. H., 1981, A&A 96, 164
Combes F. 2002, in 7th cosmology colloquium, High Energy Astrophysics, for and from Space, (arXiv:astro-ph/0208113)
Combes F., Baker, A. J., Schinnerer, E. et al. , 2009, A&A 503, 73
Combes F., García-Burillo S., Casasola V. et al. 2013, A&A 558, A124
Comte, G., Duquennoy, A., 1982, A&A 114, 7
Costagliola F., Aalto S., Rodriguez M.I et al. , 2011, A&A 528, A30
Croton D.J., Springel V., White S.D.M. et al. , 2006 MNRAS 365, 11
Dale, D.A., Gil de Paz, A., Gordon, K.D. et al. , 2007, ApJ 655, 863
Di Matteo, T., Colberg, J., Springel, V., Hernquist, L., Sijacki, D., 2008, ApJ 676, 33
Elmegreen B.G., Elmegreen D.M., 1990, ApJ 355, 52
Feruglio, C., Maiolino, R., Piconcelli, E., et al 2010 A&A 518, L155
Gao Y., Solomon P.M., 2004, ApJS 152, 63
Garcìa-Burillo, S., Combes, F., Hunt, L. K. et al. , 2003, A&A 407, 485
Garcìa-Burillo, S., Combes F., Schinnerer E., Boone F., Hunt L.K., 2005 A&A 441, 1011
Garcìa-Burillo, S., Usero A., Fuente A. et al. , 2010, A&A 519, A2
Garcìa-Burillo, S., Combes F. 2012, JPhCS Vol 372, 012050
Glass I.S. , 2004 MNRAS 350, 1049
Guilloteau, S., Lucas, R. 2000, Imaging at Radio through Submillimeter Wavelengths, 217, 299 10.
Gültekin K., Richstone, D. O., Gebhardt, K. et al. , 2009, ApJ 698, 198
Hackwell, J. A., Schweizer, F., 1983 ApJ 265, 643
Harnett J.I., 1984 MNRAS 210, 13
Harnett J.I., 1987 MNRAS 227, 887
Ho, L. C., Li, Z-Y, Barth, A. J. et al. , 2011, ApJS 197, 21
Hopkins, P.F., Quataert, E., 2010, MNRAS 407, 1529
Hopkins, P., Hernquist, L., Cox, T.J. et al. , 2006, ApJS 163, 1
Imanishi M., Nakanishi K., 2013, AJ 146, 47 & 91
Jogee S. 2006 Lecture Notes in Physics 693, 143
Korchagin, V., Kikuchi, N., Miyama, S. M. et al. , 2000, ApJ 541, 565
Kilborn V.A., Koribalski B.S., Forbes D. et al. , 2005, MNRAS 356, 77
Kohno K, Ishizuki S., Matsushita S. et al. , 2003, PASJ 55, L1
Krips M., Neri R., García-Burillo S. et al. , 2008, ApJ 677, 262
Krips M., Martn, S., Eckart, A. et al. , 2011, ApJ 736, 37

Levenson, N. A., Radomski, J. T., Packham, C. et al. , 2009 ApJ 703, 390
Malkan M., Gorjian V., Tam R., 1998 ApJS 117, 25
Martini, P., Regan, M.W., Mulchaey, J.S., Pogge, R.W. 2003a, ApJS 146, 353
Martini, P., Regan, M.W., Mulchaey, J.S., Pogge, R.W. 2003b, ApJ 589, 774
McMullin, J. P., Waters, B., Schiebel, D., Young, W., Golap, K. 2007, Astronomical Data Analysis Software and Systems XVI, 376, 127
Naylor B.J., Bradford C.M., Aguirre J.E. et al. , 2010, ApJ 722, 668
Pence W.D., Taylor K., Atherton P., 1990, ApJ 357, 415
Peeples M.S., Martini P., 2006 ApJ 652, 1097
Reif, K., Mebold, U., Goss, W. M. et al. , 1982, A&AS 50, 451
Renaud, F., Bournaud, F., Emsellem, E. et al. , 2013, MNRAS 436, 1836
Reunanen, J., Kotilainen, J. K., Prieto, M. A. 2002, MNRAS 331, 154
Reunanen, J., Prieto, M. A., Siebenmorgen, R. 2010, MNRAS 402, 879
Reynaud D., Downes D., 1998 A&A 337, 671
Riffel R.A., Storchi-Bergmann T., 2011, MNRAS 411, 469
Rupke, D. S., Veilleux, S., Sanders, D. B., 2005 ApJ 632, 751
Schmitt H., Kinney A., 1996 ApJ 463, 498
Seaquist E.R., Frayer D.T., 2000, ApJ 540, 765
Shlosman, I., Frank, J., Begelman, M. C., 1989, Nature 338, 45
Sijacki, D., Springel, V., Di Matteo, T., Hernquist, L., 2007, MNRAS 380, 877
Solomon P.M., Vanden Bout P.A. 2005, ARAA, 43, 677
Sturm, E., Gonzalez-Alfonso, E., Veilleux, S. et al. , 2011, ApJ 733, L16
Walsh, W., 2004, preprint
Wiebe, D. V., Ade, P.A.R., Bock, J. J. et al. , 2009, ApJ 707, 1809
Woo J-H., Urry C.M., 2002, ApJ 579, 530